Atmospheric Forcing of the Winter Air–Sea Heat Fluxes over the Northern Red Sea

VASSILIS P. PAPADOPOULOS,* YASSER ABUALNAJA,+ SIMON A. JOSEY,# AMY BOWER,@ DIONYSIOS E. RAITSOS,& HARILAOS KONTOYIANNIS,* AND IBRAHIM HOTEIT&

* *Hellenic Centre for Marine Research, Anavissos, Greece*
+ *Red Sea Research Centre, KAUST, Thuwal, Saudi Arabia*
# *National Oceanography Centre, Southampton, United Kingdom*
@ *Woods Hole Oceanographic Institution, Woods Hole, Massachusetts*
& *Physical Science and Engineering Division, KAUST, Thuwal, Saudi Arabia*

(Manuscript received 4 May 2012, in final form 27 August 2012)

ABSTRACT

The influence of the atmospheric circulation on the winter air–sea heat fluxes over the northern Red Sea is investigated during the period 1985–2011. The analysis based on daily heat flux values reveals that most of the net surface heat exchange variability depends on the behavior of the turbulent components of the surface flux (the sum of the latent and sensible heat). The large-scale composite sea level pressure (SLP) maps corresponding to turbulent flux minima and maxima show distinct atmospheric circulation patterns associated with each case. In general, extreme heat loss (with turbulent flux lower than -400 W m^{-2}) over the northern Red Sea is observed when anticyclonic conditions prevail over an area extending from the Mediterranean Sea to eastern Asia along with a recession of the equatorial African lows system. Subcenters of high pressure associated with this pattern generate the required steep SLP gradient that enhances the wind magnitude and transfers cold and dry air masses from higher latitudes. Conversely, turbulent flux maxima (heat loss minimization with values from -100 to -50 W m^{-2}) are associated with prevailing low pressures over the eastern Mediterranean and an extended equatorial African low that reaches the southern part of the Red Sea. In this case, a smooth SLP field over the northern Red Sea results in weak winds over the area that in turn reduce the surface heat loss. At the same time, southerlies blowing along the main axis of the Red Sea transfer warm and humid air northward, favoring heat flux maxima.

1. Introduction

The transfer of heat across the air–sea interface is a key process for ocean–atmosphere dynamics. The net air–sea heat exchange Q_{net} is the sum of four components, shortwave radiation Q_s and longwave radiation Q_b (the radiative terms) and latent heat Q_e and sensible heat Q_h (the turbulent terms),

$$Q_{\text{net}} = Q_s + Q_b + Q_e + Q_h.$$

The term Q_s represents the transfer of heat via solar radiation to the sea and is the primary source of energy for the global ocean. Part of the absorbed solar radiation is returned to the atmosphere by the infrared (longwave) radiation Q_b, yet a fraction of this radiation is scattered by the clouds and the atmospheric moisture and returns again to the sea. In contrast to Q_s, Q_b always represents heat loss by the sea. The term Q_e represents the energy transferred from the sea to the atmosphere through evaporation, and Q_h is the energy transferred as a result of the air–sea temperature difference. According to oceanographic convention, positive heat exchange values represent heat gain by the sea and vice versa. In this way, Q_s always has positive values, Q_b and Q_e have negative values, and Q_h may have positive or negative values depending on the temperature difference between air and sea.

The air–sea energy transfer affects many significant properties of both the ocean and atmosphere. Evaporation, sea surface temperature variability, and near–boundary layer stability of the air and the seawater columns are directly related to surface heat fluxes. On a global scale, air–sea heat exchange is a significant factor influencing the weather and, on longer time scales, the climate regime. On the other hand, atmospheric circulation on various spatial and temporal scales affects the surface

Corresponding author address: Vassilis P. Papadopoulos, Hellenic Centre for Marine Research, Institute of Oceanography, 46,7 Km Athinon-Souniou Ave., Anavissos, Attica 19013, Greece.
E-mail: vassilis@hcmr.gr

DOI: 10.1175/JCLI-D-12-00267.1

energy exchange (Cayan 1992; Alexander and Scott 1997; Bond and Cronin 2008; Shaman et al. 2010; Josey et al. 2011; Papadopoulos et al. 2012a,b,c). From an oceanographic point of view, the air–sea heat exchange regulates the warming/cooling of the sea surface layers, thus fuelling the oceanic thermohaline circulation. In particular, extreme surface cooling is a major precondition in triggering the vertical conveyor belt, a crucial oceanic feature that renews the deep waters and oxygenates the near-bottom marine environment. Ongoing global warming favors positive surface buoyancy and renders the study and monitoring of deep convection events more significant as a possible retarding of such events would evoke dramatic changes, in particular to marine ecosystems.

The Red Sea is an elongated basin lying between northeastern Africa and the Arabian Peninsula and spans almost 20° in latitude from 12° to 30°N with a length exceeding 2000 km and a maximum width around 350 km. The Red Sea is a semienclosed marginal sea and communicates with the open Indian Ocean through the narrow Strait of Bab el Mandeb located at its southernmost edge. To the north, the artificial Suez Canal connects the Red Sea with the Mediterranean Sea, yet the amount of water exchange through the long narrow channel is practically negligible. Surrounded by arid or semiarid land, the Red Sea is characterized by extremely low precipitation, a lack of river runoff (Morcos 1970; Eshel et al. 1994), and an extremely high evaporation rate that exceeds 200 cm yr^{-1} (Morcos 1970; Sofianos et al. 2002). The water deficit caused by the evaporation excess is counterbalanced by a net inflow of relatively fresh Indian Ocean water at the Strait of Bab el Mandeb (Murray and Johns 1997; Sofianos and Johns 2002; Aiki et al. 2006). The entering Indian Ocean water flows northward at the surface becoming gradually saltier with salinity exceeding 40 over the northern Red Sea. Eventually it sinks during winter, through a mechanism that still remains unresolved, over the northern part of the Red Sea to form the Red Sea Outflow Water (RSOW) and the Red Sea Deep Water (RSDW). The RSOW is formed in the open northern Red Sea (Eshel and Naik 1997, Sofianos and Johns 2007) and the RSDW is believed to be formed by a near-bottom advection of very saline and relatively cold seawater of Suez and/or Aqaba Gulf origin (Wyrtki 1974; Cember 1988; Woelk and Quadfasel 1996; Clifford et al. 1997; Plähn et al. 2002; Biton and Gildor 2011). Both water masses, RSOW and RSDW, are vital for the Red Sea ecosystem providing ventilation to the intermediate and deep layers, thus preventing anoxic conditions. In particular, the RSOW flows out to the Indian Ocean (Bower et al. 2000, 2005; Aiki et al. 2006) and is traced as a maximum salinity intermediate water in the northwestern Indian Ocean, reaching as far as the southeastern coast of Africa (Fine et al. 1988; Beal et al. 2000). However, several studies based on modeled and remotely sensed datasets show that global warming and climate change trends are particularly evident in the Red Sea (Kleypas et al. 2008; Cantin et al. 2010; Raitsos et al. 2011). This could potentially lead to fewer convection events because of positive surface buoyancy.

The knowledge of the air–sea heat flux regime over the Red Sea is poor and limited to the estimation of the entire basin annual heat budget. Two studies carried out by Tragou et al. (1999) and Sofianos et al. (2002), using different methodological approaches, result in a basin net heat loss between 8 and 11 W m^{-2}. However, the spatiotemporal characteristics of the surface heat exchange and the atmospheric forcing that directly drives the heat flux remain practically unexplored. The study at hand investigates the influence of the atmospheric circulation on the turbulent heat flux variability over the northern part of the Red Sea. Our analysis focuses on the high-frequency variability of the air–sea heat exchange using variations in the daily sum of latent heat and sensible heat fluxes as a proxy for variability in the surface heat exchange. The daily variability is considered an advisable time scale, since the time required for buoyancy loss of the surface layer is much shorter (Leaman and Schott 1991). Both high- and low-frequency variability are likely to affect the surface fluxes regime. For example, successive events of extreme heat loss by means of turbulent fluxes can contribute to a remarkable negative monthly-mean flux anomaly. Nevertheless, over regions like the northern Red Sea, which are characterized more or less by a stable weather regime (Patzert 1974; Jiang et al. 2009), the short-period extreme events can be obscured under the low-frequency monthly or seasonal time scales. An example of short-period wintertime events is the strong westward-blowing wind jets, which occur every 10–20 days along the northeastern Red Sea coastline. These dry and relatively cold wind jets are considered a favorable factor in triggering deep convection over the northern Red Sea (Jiang et al. 2009). The above factors motivate us to study the atmospheric forcing that favors deep- and intermediate-water convection over the northern Red Sea. In addition, our findings may provide a useful background, enabling better evaluation of projected climate scenarios for the region.

The manuscript is structured as follows: the datasets employed and the methodological approach are discussed in section 2. Section 3 provides the climatology of the air–sea heat fluxes over the entire Red Sea Basin. In section 4, we analyze the large-scale atmospheric circulation patterns, in terms of composite sea level pressure

(SLP) maps derived for the low and high surface flux regimes. Section 5 presents individual SLP maps and the associated wind fields for these extremes. Section 6 investigates the temporal characteristics of the outmost events. Finally, section 7 contains some concluding remarks and points out some major issues needing further investigation.

2. Datasets and methodology

a. The datasets

Daily values for Q_e and Q_h are obtained from the objectively analyzed air–sea fluxes dataset (OAFlux; Yu et al. 2008) of the Woods Hole Oceanographic Institution. The radiative terms are also taken from the OAFlux archive, but they are produced from the International Satellite Cloud Climatology Project Flux Data (ISCCP-FD) using a radiative transfer model from the Goddard Institute for Space Studies (Zhang et al. 2004). The obtained ISCCP-FD from the OAFlux archive are daily averaged and linearly interpolated from their original 2.5° × 2.5° resolution onto a 1° × 1° grid to coincide with the turbulent fluxes data. The turbulent terms span the period 1985–2011 and the radiative terms span the period 1983–2009. Daily SLP, covering a broad area extending from 40°W to 120°E in longitude and from 20°S to 70°N in latitude with a resolution of 2.5°, for the 27-yr period of 1985–2011, is taken from the National Centers for Environmental Prediction–National Center for Atmospheric Research (NCEP–NCAR) reanalysis dataset (Kalnay et al. 1996). In addition, we use daily 10-m wind fields from the full-resolution (1° × 1°) European Centre for Medium-Range Weather Forecasts (ECMWF) Interim Re-Analysis (ERA-Interim) dataset (Dee et al. 2011).

b. Methodology

The present article aims to investigate the atmospheric forcing on the winter air–sea heat flux variability over the northern part of the Red Sea. Our study focuses on the turbulent terms, latent and sensible heat, since they exhibit considerably higher variability than the radiative terms (details are given in section 3). First, we present a general climatology of the heat fluxes covering the entire basin and we demonstrate the differences between the northern and the southern parts of the Red Sea. Next, we investigate the variability in the fluxes over the northern part of the Red Sea by using the standard deviation of the two different terms. The standard deviation is derived by the heat flux anomalies in respect to the long-term monthly means. The variability over this part of the Red Sea is of particular interest as intermediate- and deep-water formation may occur here during winter. The winter [December–February (DJF)] daily sums of latent and sensible heat at the grid points north of the 25th parallel are taken into account. The criterion of 25th parallel is based on the main outputs of previous studies identifying the region north of this parallel as the potential intermediate- and deep-water convection area (Eshel and Naik 1997; Sofianos and Johns 2003, 2007). Interestingly, the results are the same even if we use the boundary of the 23rd or 27th parallels, indicating that cases of strong atmospheric forcing are characterized by uniform conditions over an extensive area of the northern Red Sea. A composite time series of winter daily values is formed averaging 11 gridpoint values (Fig. 1). By using averaged values, we prevent possible biases derived from potential local effects that can appear under specific conditions and ensure at the greatest level the ability of the derived time series to capture events of maximum spatial influence over the examined area. However, as most of the used grid points are very close to land, there could be an issue on how biased their corresponding values are because of the land–ocean transition. The dataset used in the present study spans a relatively recent period in which all the

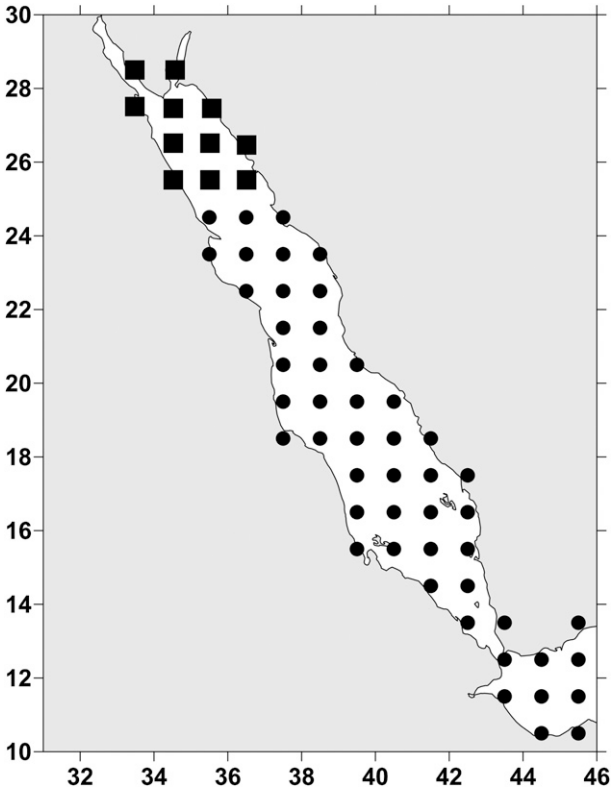

FIG. 1. The Red Sea Basin and the OAFlux grid points (squares) used in our analysis of turbulent heat loss variability. We segregate the area north of the 25th parallel. The total number of grid points is 11.

modern-era available tools (satellite observations, numerical weather predictions, and real measurements) are utilized (Yu et al. 2008). For this reason, a better data quality is expected, and actually near-land OAFlux data have been qualified as well performed over a frequent land–ocean transition region in the eastern Mediterranean Sea (Papadopoulos et al. 2010).

To investigate the atmospheric controls on the heat flux variability, we segregate out the 5% lowest and highest daily values during winter for the period 1985–2011. Values included within the lowest and highest 5th percentiles are less than -380 W m^{-2} and greater than -100 W m^{-2}, respectively. For these outmost values (events), we average the corresponding SLP to produce composite maps in order to demonstrate the general atmospheric circulation patterns that favor the lowest/highest turbulent flux values. The examined SLP field covers a broad area extending from 40°W to 120°E in longitude and from 20°S to 70°N in latitude. In addition, we present the SLP anomaly (SLPA) maps for the turbulent flux minima and maxima and investigate the potential relation of the SLPA patterns with the modes of SLP variability. The latter are obtained using EOF analysis and the EOF maps are presented as homogeneous correlation maps (Bjornsson and Venegas 1997). The SLPA used in composites and EOF analysis is taken after removing the corresponding long-term monthly means at each grid point. The composite maps provide the general tendency of the atmospheric circulation during the extremes, yet the composites themselves may never be identical with individual daily maps corresponding to turbulent flux extremes. Therefore, we also present the standard deviation of the composite maps and we further describe some of the specific daily SLP maps that correspond to the lowermost and uppermost values of the grid-averaged turbulent flux. To highlight the wind effects, we present the daily wind field for the lowest and highest extremes, thus showing the differences in wind conditions prevailing during the lower and upper turbulent flux values. Last, we examine the temporal variability of the winter turbulent flux extremes and analyze their trends taking into account the extreme deciles and the lowest and highest fifth percentiles. Particular attention is given to the trend of the extremes that is analyzed using the Mann–Kendall nonparametric test (Mann 1945; Kendall 1975) and linear regression.

3. Red Sea heat flux climatology

To demonstrate the different spatial characteristics of the turbulent and radiative terms of the air–sea heat fluxes, we present separately for each term their annual and winter climatology and standard deviation maps. Figure 2a presents the annual mean of the turbulent components. The heat loss is lower over the southern basin with values around -100 W m^{-2} and higher, around -180 W m^{-2}, over the northern Red Sea. These values and their spatial distribution are consistent with turbulent flux climatology derived using several databases (see Fig. 2 of Yu et al. 2007). Turbulent fluxes over the southern basin exhibit also slightly lower standard deviations than over the northern basin (Fig. 2b). The winter climatology takes into consideration the months December, January, and February. During winter, the contrast between the northern and the southern basin is obvious. As expected, the northern basin exhibits much higher heat loss with mean values locally stronger than -250 W m^{-2}, whereas significantly lower heat loss around -50 W m^{-2} is observed over the southernmost Red Sea (Fig. 2c). Standard deviation values are also much higher in the north, particularly north of the 25th parallel, indicating a higher variability compared to the south (Fig. 2d). Moreover, winter standard deviations over the northern basin exhibit even higher values compared to the annual ones. Higher standard deviations suggest the occurrence of large departures from the mean values that in the case of negative anomalies can create favorable conditions for intermediate/deep convection events.

The radiative terms have a similar spatial distribution to the turbulent terms with the exception of larger variability occurring over the southern basin. The mean $Q_s + Q_b$ values range from around 120 W m^{-2} in the north to higher than 150 W m^{-2} over the central southern basin (Fig. 3a). Again, this is in accordance with most of the examined databases in the study of Yu et al. (2007). The standard deviation exhibits a rather complex spatial distribution, yet the highest values are clearly observed in the southern basin (Fig. 3b). Winter means are expectedly lower than annual means, especially over the northern basin, showing a typical zonal gradient (Fig. 3c). In contrast to the turbulent terms behavior, the winter standard deviation map is smoother compared to the annual map (Fig. 3d). Clearly, over the northern basin, the winter radiative terms exhibit much lower values and much lower variability ($<$10 W m^{-2} standard deviation) compared to the turbulent terms (up to 50 W m^{-2}). Furthermore, over the neighboring eastern Mediterranean (southern Aegean and Levantine Seas), the radiative terms display a negligible contribution to the total energy anomaly required to produce extreme events (Papadopoulos et al. 2012b). For these reasons, we choose to study the atmospheric forcing of the heat exchange during winter using the daily turbulent flux variability as a proxy for the net flux. This is particularly appropriate for heat loss extreme events when daily

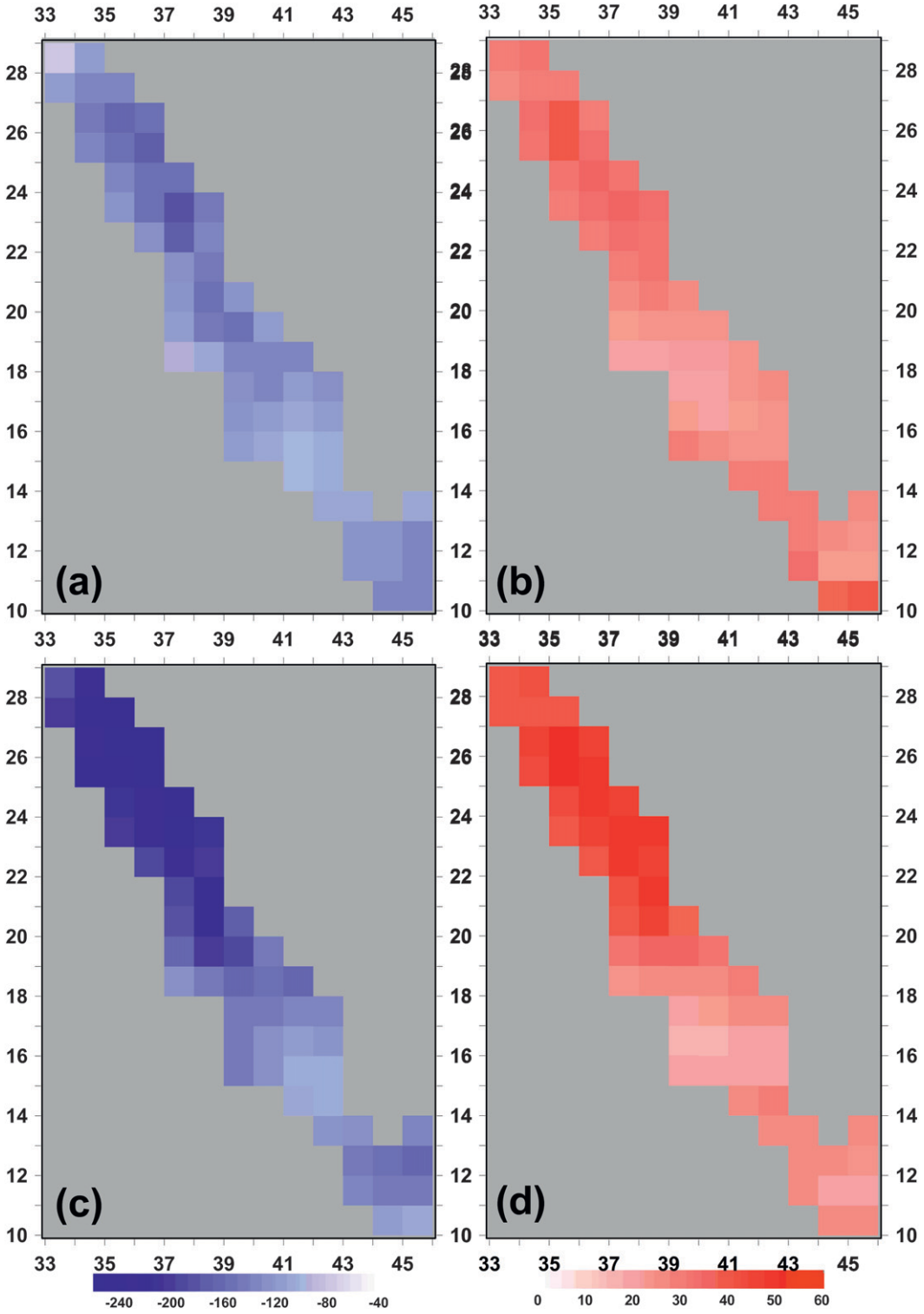

FIG. 2. Annual OAFlux (a) climatology and (b) standard deviation of the turbulent terms (the sum of latent and sensible heat; W m^{-2}). (c),(d) As in (a),(b), but for the winter months only (DJF) derived from daily values for the period 1985–2011.

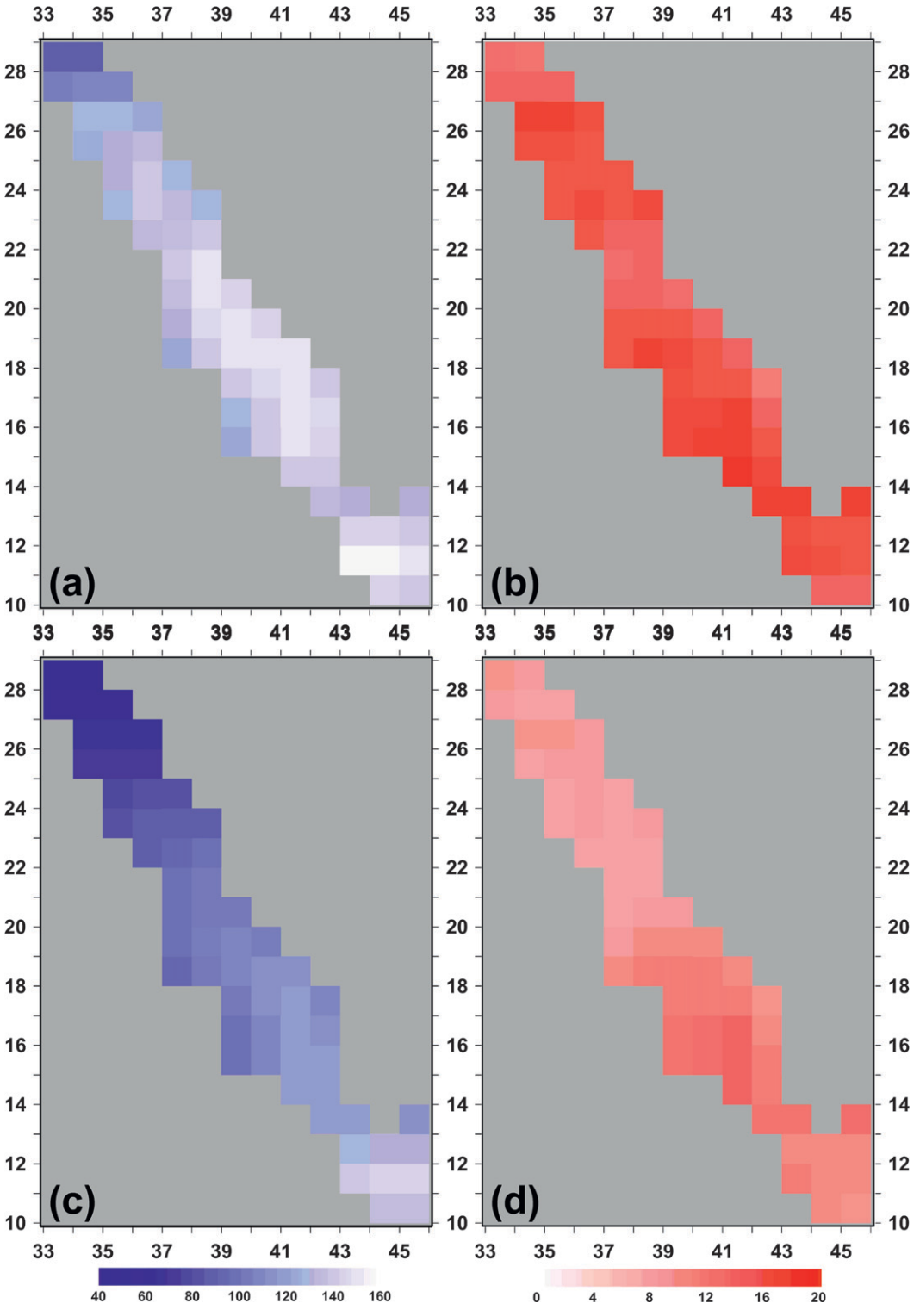

FIG. 3. ISCCP (a) climatology and (b) standard deviation of the radiative terms (the sum of shortwave and longwave radiation; W m^{-2}). (c),(d) As in (a),(b), but for the winter months only (DJF) derived from daily values for the period 1983–2009.

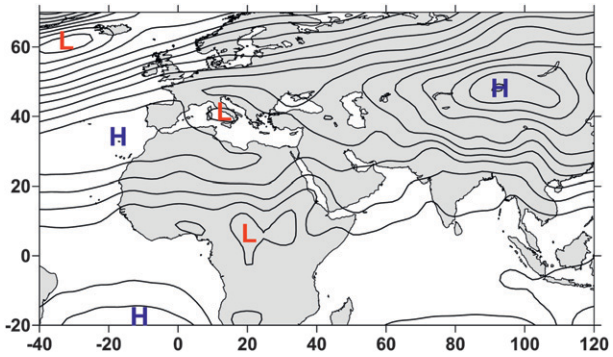

FIG. 4. Winter (DJF) SLP climatology derived from daily NCEP–NCAR values for the period 1985–2011.

values of the turbulent terms lower than -400 W m^{-2} can be frequently observed over the northern Red Sea.

4. The composite SLP maps

The influence of large-scale atmospheric circulation is depicted through composite SLP maps that correspond to the lowest and highest 5th percentiles (5%) of the winter daily turbulent flux values. To obtain a background, the mean winter (DJF) SLP map is presented in Fig. 4. The Red Sea is mainly affected by the equatorial African low pressure system and the projection of the strong winter central Asia high, whereas the central Mediterranean low may play a key role on the pressure gradient over the northern part of the basin. These three barometric systems are expected to influence the northern Red Sea SLP regime according to their position and intensity. The winds related to a specific SLP gradient are strongly modified by the local orography, which results in winds blowing along the main axis of the Red Sea or cross-axis winds channeled through numerous mountain gaps (Patzert 1974; Jiang et al. 2009).

Figure 5a shows the composite SLP map corresponding to the lowest 5% (i.e., most extreme heat loss) of the daily turbulent flux values over the northern Red Sea during winter. The most conspicuous feature is the eastward extension of the Azores anticyclone jointly with the westward extension of the Siberian high covering with high pressure a broad area from the Azores Islands to eastern Asia. In particular, the anticyclone over Turkey creates the requisite SLP gradient for transferring continental, cold, and dry air masses over the northern part of the Red Sea. The flow of cold and dry winds over the warm Red Sea waters increases the heat loss from the sea surface through the extremely low turbulent flux values. As a consequence, these conditions are favorable to triggering intermediate/deep-water formation. The SLP field of Fig. 5a may never coincide with the daily maps that are merged to produce the composite. For this reason, the spatial distribution of the standard deviation depicting the variability of the merged maps (Fig. 5b) is of high importance. The striking characteristic of this map is the large fluctuation

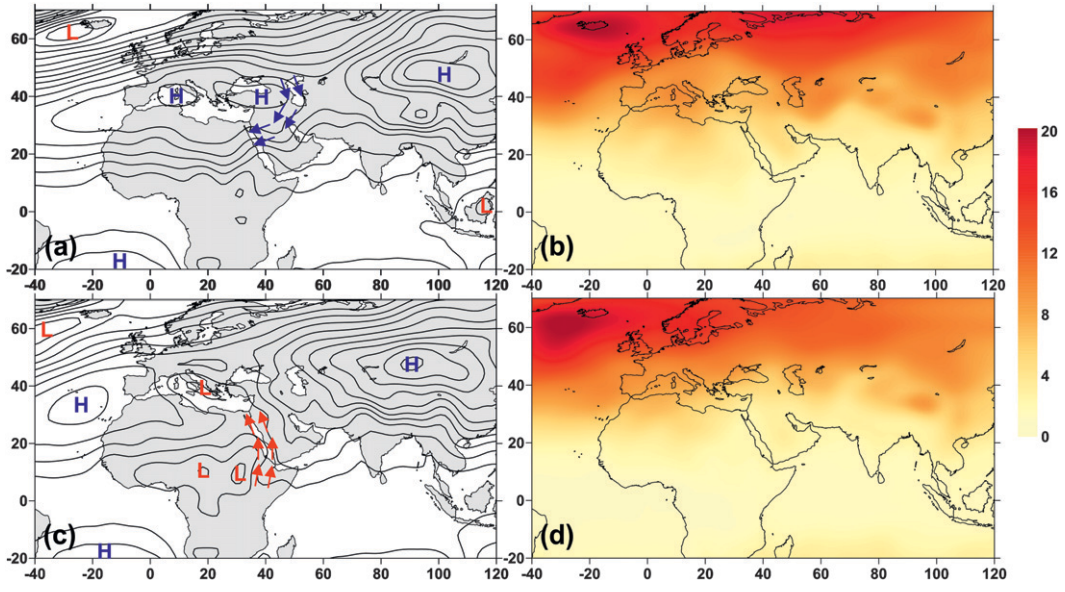

FIG. 5. Composite SLP maps for the (a) lower and (c) upper 5% of the winter (DJF) daily latent heat (LH) + sensible heat (SH) during the period 1985–2011 over the northern part of the Red Sea and (b),(d) the standard deviation (hPa) of the set of individual maps used to form the composite map. Manually drawn blue and red vectors indicate the potential air mass transfer.

over the higher latitudes in contrast to the stability of the equatorial area. The relatively low variability over the eastern Mediterranean Sea, northeastern Africa, and almost the entire Red Sea indicates consistency of the lower-atmospheric circulation over these regions when enhanced heat loss occurs in the northern Red Sea. The SLP over the three aforementioned areas determines by nature the SLP gradient over the northern Red Sea.

The composite SLP for the highest 5% (i.e., weakest heat loss) of the turbulent flux values (Fig. 5c) exhibits obvious differences compared to that corresponding to the lowest values. The weakest heat loss occurs when low pressures prevail over the eastern Mediterranean and equatorial Africa. The eastern Mediterranean low divides the broad anticyclone of the previous map into the typical Azores high (subtropical North Atlantic anticyclone) and the winter central Asia anticyclone. This SLP configuration is associated with a smooth SLP field over the northern Red Sea and a general atmospheric circulation that favors the transfer of warm and moist air masses from the southern Red Sea Basin. The smooth SLP causes low wind speed, a determinant factor for the weak turbulent fluxes magnitude. The combination of weak winds with warm and moist air reduces noticeably the heat loss through the turbulent fluxes and leads to positive air–sea heat exchange anomalies (i.e., reduced heat loss). The standard deviation of the weak heat loss composite (Fig. 5d) again exhibits larger SLP variation over the high latitudes, decreasing gradually southward. As noticed for the standard deviation of the strong turbulent flux composite, the eastern Mediterranean Sea, northeastern Africa, and the entire Red Sea again show relatively low variability: that is, a steady SLP field exists over these areas.

Figure 6 presents the SLP departures (SLPA) from the mean (Fig. 4) corresponding to the two composites. In the case of the lowest 5th percentile of the turbulent flux values over the northern Red Sea (Fig. 6a), a wavelike structure is identified. This almost zonal wavelike pattern exhibits four prominent ''centers of action'' with phase alternation, with the first over the North Atlantic Ocean; the second over the eastern Mediterranean Sea, Turkey, northeastern Africa, and the northern Arabian Peninsula; the third over west-central Asia; and the forth over northeastern Asia. Similar centers of action appear in the case of the highest 5th percentile (Fig. 6b), yet with a phase inversion and slightly weaker anomalies in comparison to the lowest extremes. In both extremes, the key center of action for the northern Red Sea turbulent fluxes is the second one that appears over the eastern Mediterranean, Turkey, Middle East, and northeastern Africa. This center is a part of a successive seesaw teleconnection, indicating a strong relation between a wave train–like

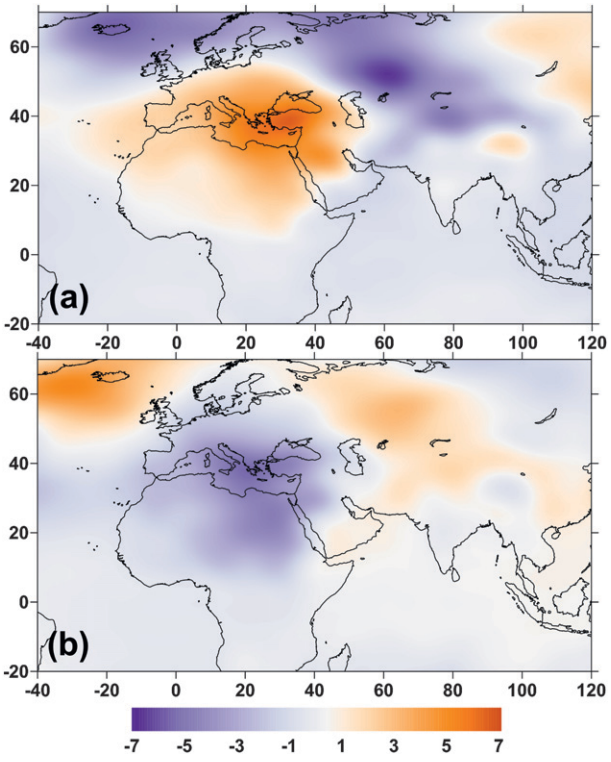

FIG. 6. Composite SLP anomaly (hPa) for the (a) lower and (b) upper 5% of the winter (DJF) daily LH + SH during the period 1985–2011 over the northern part of the Red Sea.

SLPA pattern and the turbulent flux variability over the studied area during the extremes. Next, we investigate the potential connection of this wave train pattern with the modes of variability of the SLP using EOF analysis. We apply the EOF analysis to the daily SLP fields during winter. Figure 7 shows the first six EOF modes of the SLP and the associated explained variance. Visually, the presented modes exhibit no strong similarities with the SLPA patterns, and this is corroborated to some extent by the spatial correlation coefficients calculated in pairs between SLPA and EOF maps as presented in Table 1. However, EOF1, EOF3, and EOF5 have higher correlation values, which suggests that the derived SLPA patterns could be reproduced by a combination of these modes.

5. Individual SLP maps and the wind effect

As mentioned previously, the composite SLP maps, though very useful to identify the general pattern of the large-scale lower-atmospheric circulation, may never appear the same as the individual daily maps. Therefore, we examine the individual daily SLP maps that correspond to the eight lowest (bottom 8) and highest eight (top 8) turbulent flux values over the northern Red Sea.

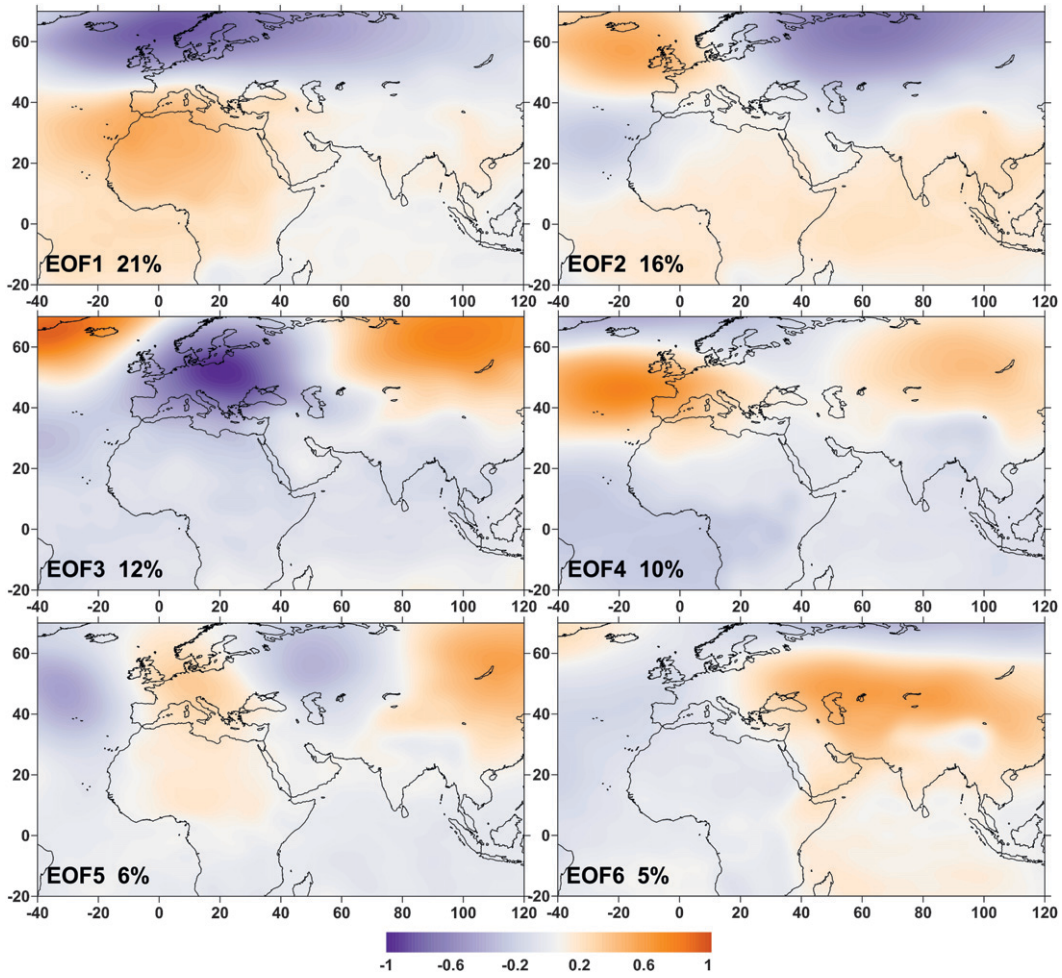

FIG. 7. The first six EOF modes of the winter SLP. The percentage denotes the fraction of the explained variance.

All of the bottom-8 daily values are less than -500 W m^{-2}, while top-8 daily values are greater than -50 W m^{-2}. In addition, to demonstrate the primary role of the wind regime, we display for the bottom-4 and top-4 cases the daily wind field that prevails during these events. The SLP maps of Fig. 8 portray eight more or less dissimilar SLP configurations that produce extremely low turbulent fluxes over the northern part of the Red Sea basin. However, in all of these maps we find one or more of the features that characterize the composite corresponding to the lowest 5th percentile (Fig. 5a). The relatively high pressure field, usually as a subcenter of the midlatitude extended anticyclone over the eastern Mediterranean Sea region, is the most consistent feature. This feature generates the prerequisite SLP gradient over the studied area, which in turn results in strong wind magnitudes. Furthermore, the equatorial African lows are weaker and appear to be of limited size. In each case, the general atmospheric circulation advances the transfer of cold and dry air masses over the studied area with the possible streamflow indicated by the manually drawn thick blue lines. Wind fields during extreme surface cooling are consistent with these airmass routes (Fig. 9), showing that in general the prevailing winds to have a more or less significant negative meridional component (v component) over the northernmost part of the Red Sea. It has to be noted that the resolution of 1° is rather too coarse to reproduce precisely the complex localized orography effects described in Jiang et al. (2009). In this way, the possibility of much stronger localized winds is very high for all of the presented cases, especially for the

TABLE 1. Spatial correlation coefficients between SLPA and EOF maps. SLPA-bot and SLPA-top refer to the composite maps of SLP anomaly (hPa) for the lower and the upper 5% of the daily LH + SH, respectively.

Map	EOF1	EOF2	EOF3	EOF4	EOF5	EOF6
SLPA-bot	0.63	0.16	−0.33	0.15	0.37	−0.19
SLPA-top	−0.54	0.09	0.49	0.07	−0.39	0.32

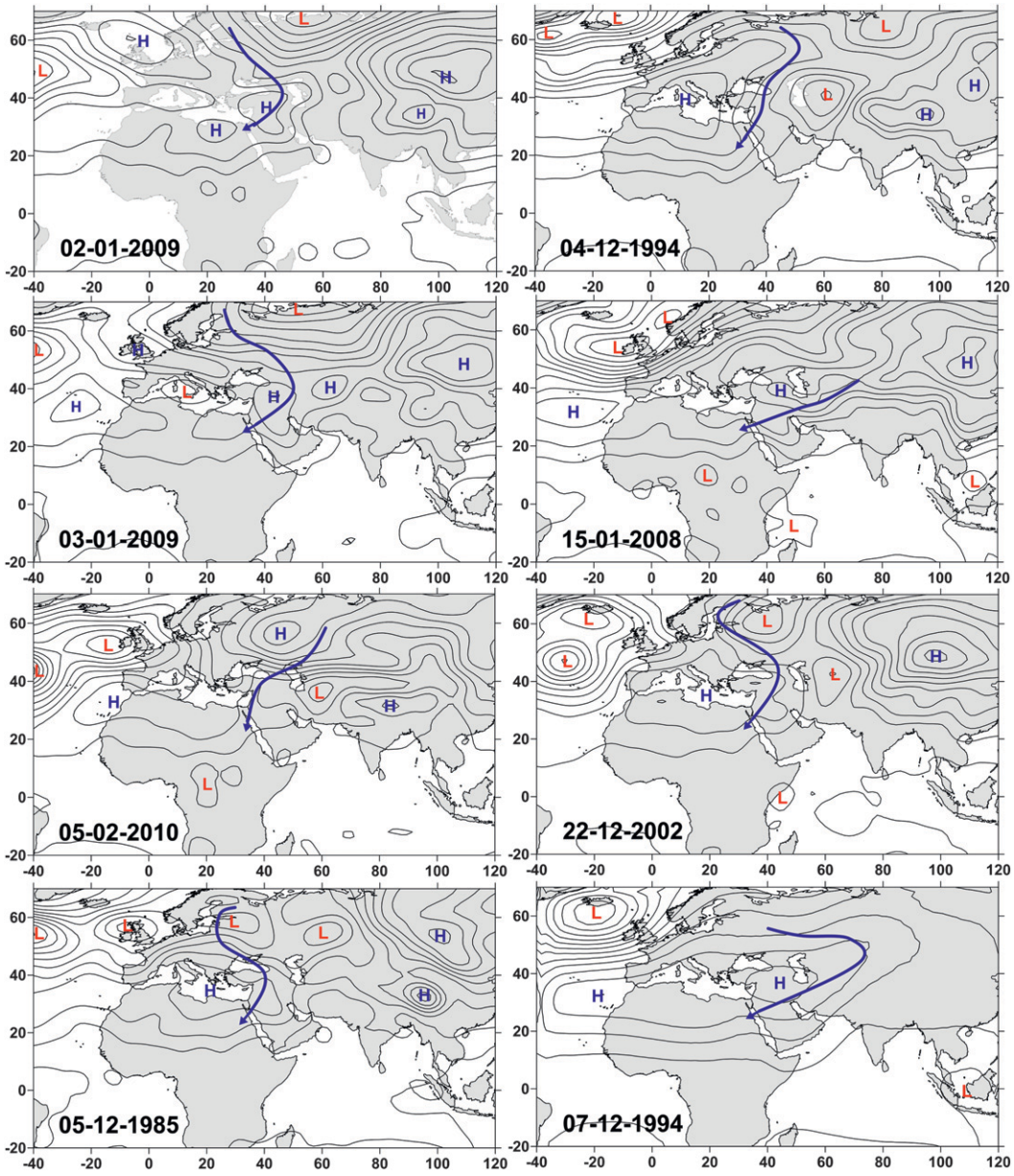

FIG. 8. Synoptic SLP maps (with the corresponding dates) during the eight lowest daily winter LH + SH values. Manually drawn thick blue lines show schematically the potential airmass routes toward the northern part of the Red Sea.

cases of the bottom panels of Figure 9 that show winds blowing from land to sea. In such cases, the coastal mountain gap channels winds that can locally attain speeds over 15 m s^{-1} increasing significantly the evaporation and cooling substantially the sea surface (Jiang et al. 2009).

Conversely, the daily SLP maps for the positive turbulent flux anomalies (Fig. 10) show a much smoother pressure gradient over the northern Red Sea and/or a general northward airflow as the thick red lines (manually drawn) demonstrate. Almost all of the maps show a smooth SLP field over the studied area that implies a weak wind field, which in turn generates the positive turbulent flux anomalies (note that, with our sign convention, positive anomalies are associated with weaker heat loss values). The extended midlatitude high pressure area associated with the negative anomalies is either divided into the typical Azores and Siberian highs by low pressure insertion over the eastern Mediterranean or is confined eastward to the Siberian high. In addition, the permanent equatorial African low is now much broader and extended to reach the African coast

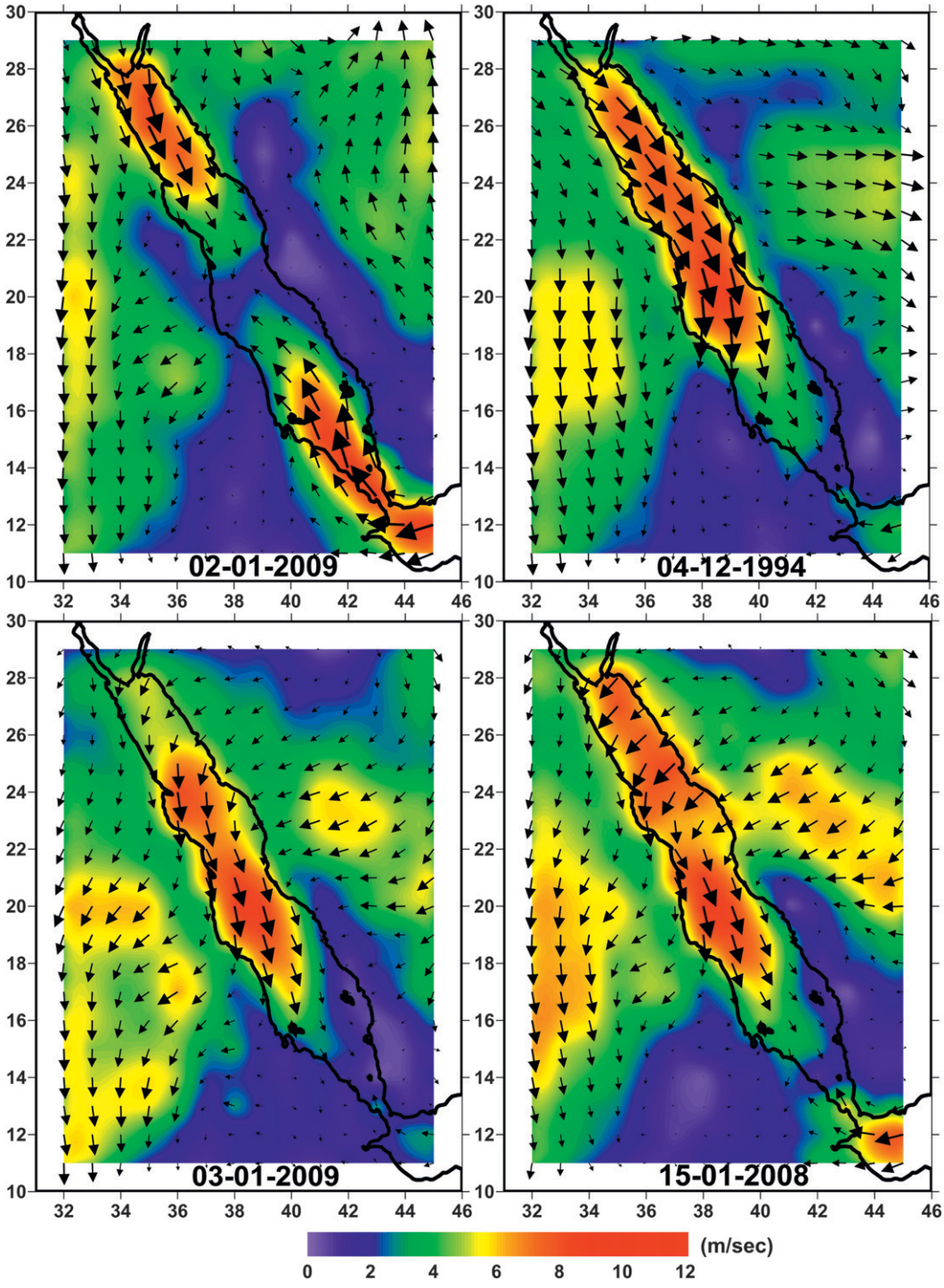

FIG. 9. Surface wind field (10 m) over the Red Sea corresponding to the first four lowest (negative anomalies) daily winter LH + SH values.

of the Red Sea favoring a general southerly wind over the main axis of the Red Sea. This type of lower-atmospheric circulation can transfer warm, humid air over the northern Red Sea, contributing to lower evaporation and potential heat gain by the sea through the sensible heat flux (for the case where the air is warmer than the sea surface). Winds are extremely weak over the northern half of the basin as it is shown on the

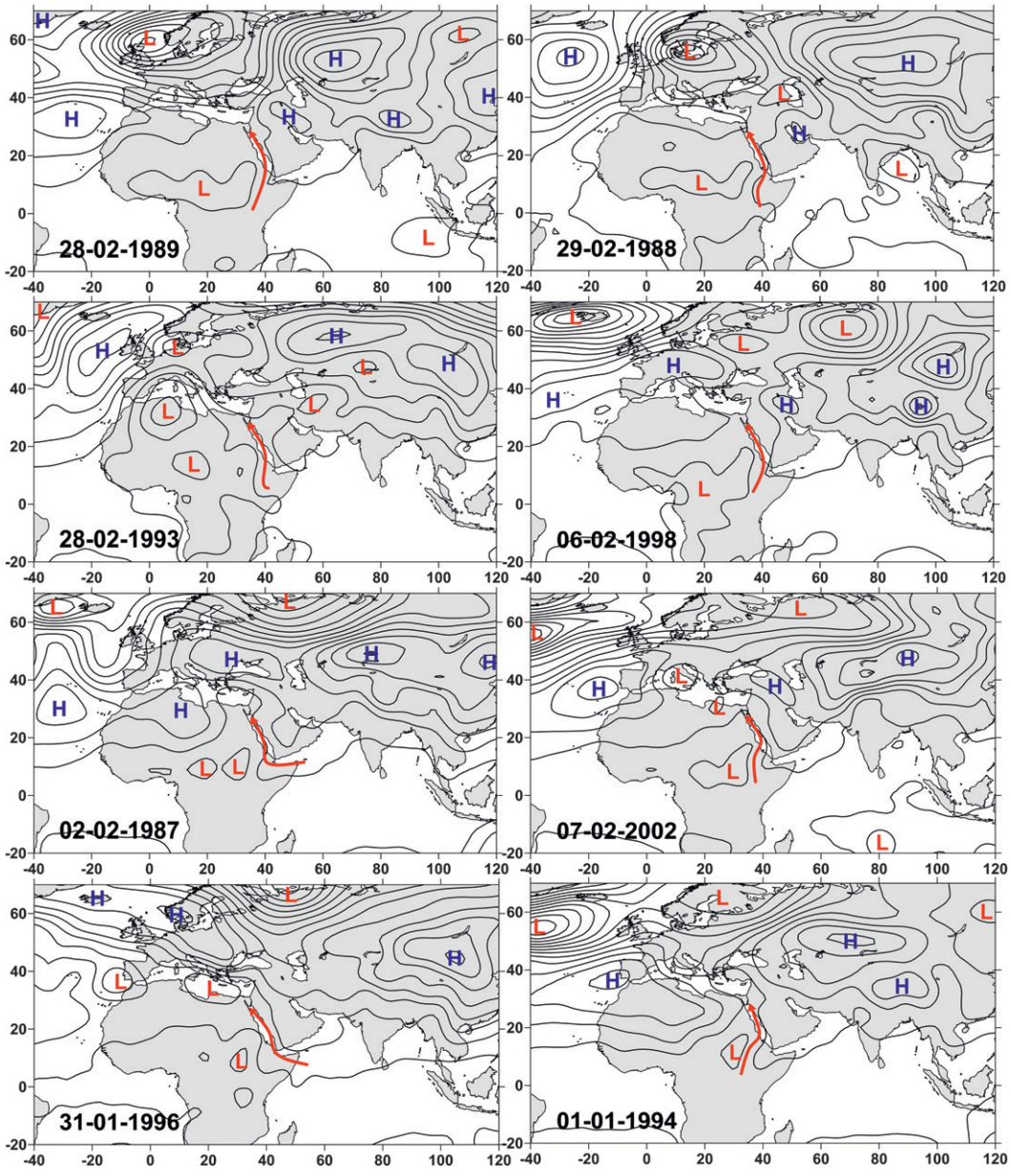

FIG. 10. Synoptic SLP maps (with the corresponding dates) during the eight highest daily winter LH + SH values. Manually drawn thick red lines show schematically the potential airmass routes toward the northern part of the Red Sea.

top-4 wind maps (Fig. 11). All of these cases except the first (Fig. 11, top-left panel) show the aforementioned along-axis northward flow over the southern half of the entire basin. A striking feature of the wind maps is the relatively windy southern half in contrast to the calm northern half. Again, the relatively low-resolution wind data prohibit a sufficiently detailed wind field, which would provide a more explanatory picture including potential localized wind effects in magnitude and direction and their influence on air–sea heat flux variability over the northern part of the basin.

6. Temporal characteristics of the extremes

Finally, we study the temporal distribution of the extreme turbulent flux values investigating two outmost percentiles, the upper and lower decile (10%) and the 5th percentile of the total daily turbulent flux values during the winter months for the 27-yr period of 1985–2011. The time variation of the daily turbulent flux is shown in Fig. 12 (top). The red line corresponds to a negative linear regression trend. The negative trend indicates a decrease of the turbulent flux value (heat

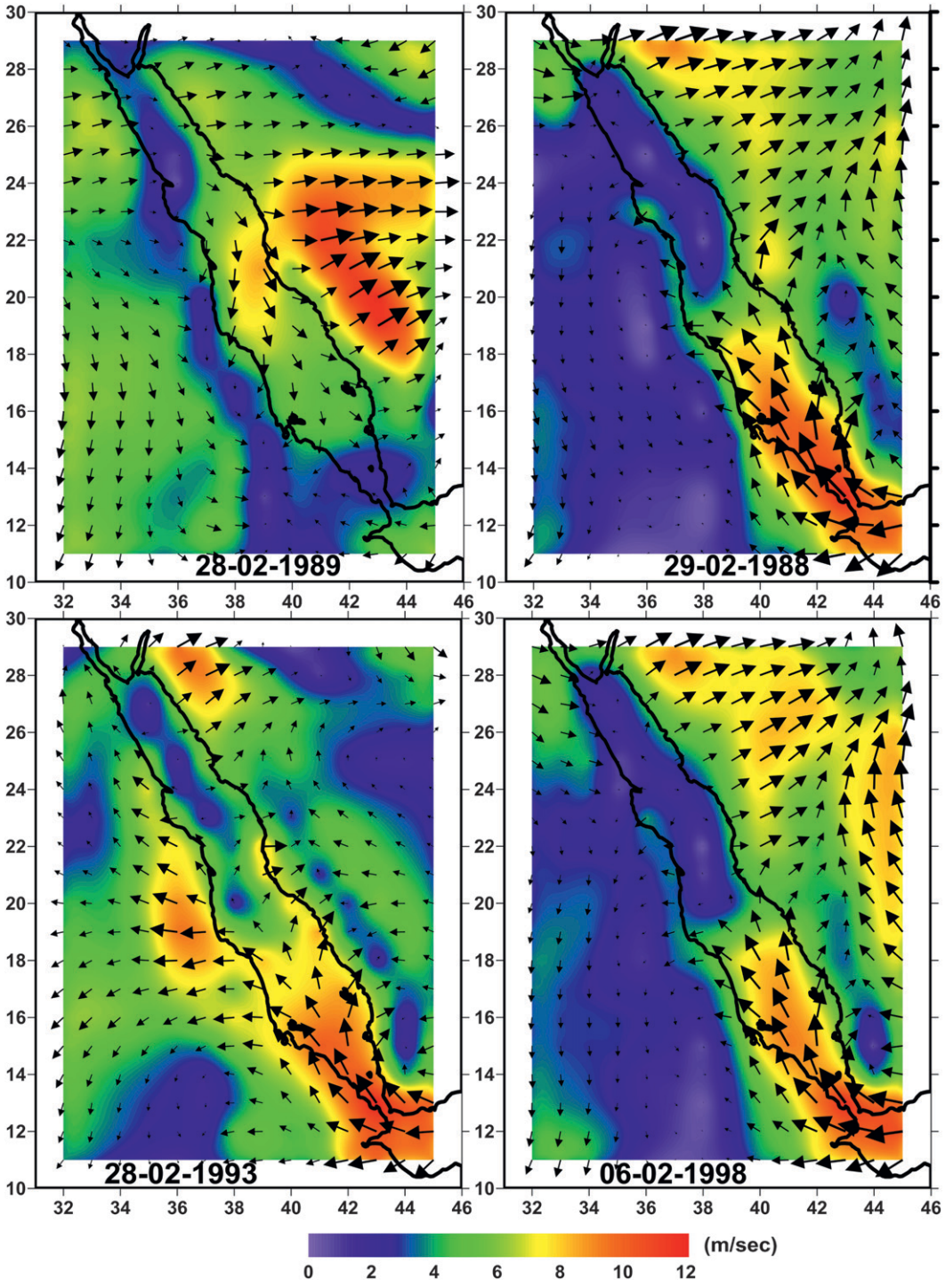

FIG. 11. Surface wind field (10 m) over the Red Sea corresponding to the first four highest (positive anomalies) daily winter LH + SH values.

loss enhancement) over the examined wintertime by 2.3 W m^{-2} yr^{-1}. The Mann–Kendall test shows that the trend is not significant at a confidence level of 95%. Note that Raitsos et al. (2011) identify a positive sea surface temperature (SST) trend during nearly the same period (1985–2007), which is consistent with the heat flux trend if the increase in SST is a driving factor for the increased heat loss. Model studies suggest that the surface

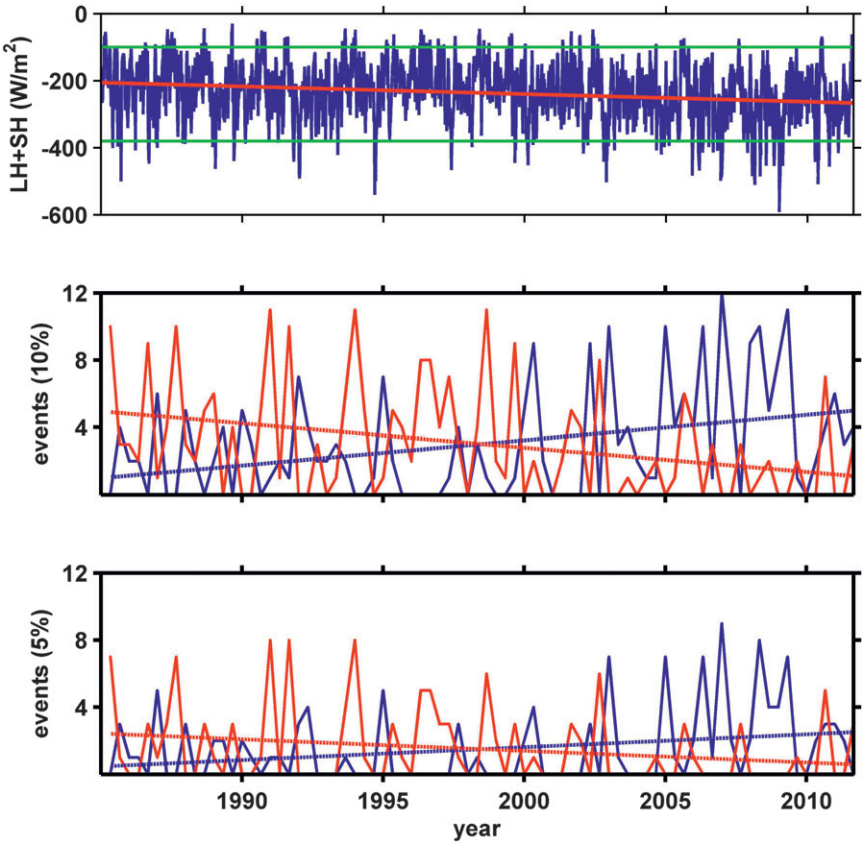

FIG. 12. (top) LH + SH values during winter and the corresponding linear trend line for the period spanning January 1985–February 2011. Green lines mark the thresholds for lower and upper 5%. (middle) Monthly number of events (i.e., days) with sum of the LH + SH values included in the lower (blue) or upper (red) 10% of the DJF daily net heat flux distribution for all years. Blue and red lines are the corresponding linear trend lines (least squares). (bottom) As in (middle), but with 5% limit.

water travels to the northern basin from the far south through a complex surface circulation pattern (Eshel and Naik 1997; Sofianos and Johns 2003). Thus, it is possible that positive SST anomalies could have been produced in lower latitudes and advected to the northern Red Sea. This is particularly evident based on the SST trend analysis carried out by Raitsos et al. (2011). They identified an abrupt surface warming over the entire basin after 1994, but the southern and the central Red Sea showed much stronger positive SST anomalies in comparison with the northern part (see Fig. 1b of Raitsos et al. 2011). To quantitatively examine the above assumption we calculate the turbulent fluxes using the state-of-the-art Coupled Ocean–Atmosphere Response Experiment (COARE), version 3, algorithm (Fairall et al. 2003). We calculate the difference in the sum of latent and sensible heats corresponding to a difference of 1° in SST when the rest of the variables remain constant. For example, with typical values of an SLP of 1010 hPa, a wind speed of 8 m s^{-1}, a T_{air} of 18°C, and a specific humidity of 2 g kg^{-1}, the turbulent fluxes are lower (enhanced heat loss) by more than 60 W m^{-2} if the SST is 25°C instead of 24°C.

Figure 12 (middle) shows the time variation of the monthly number of events (days) included in the upper and lower deciles of the turbulent flux values. For both of these cases, the trend (regression for the upper decile shown with a red line and for the lower decile shown with a blue line) is significant at the 95% confidence level. These findings are consistent with the negative trend of the turbulent flux values discussed in the previous paragraph. As expected, the two trends are inversely related since events of heat loss maxima exhibit a higher frequency with time, while the opposite occurs for the number of heat loss minima during the last 27 yr (from January 1985 to February 2011). The majority of months with events of heat loss minima have either no heat loss maxima events or both numbers, minima and

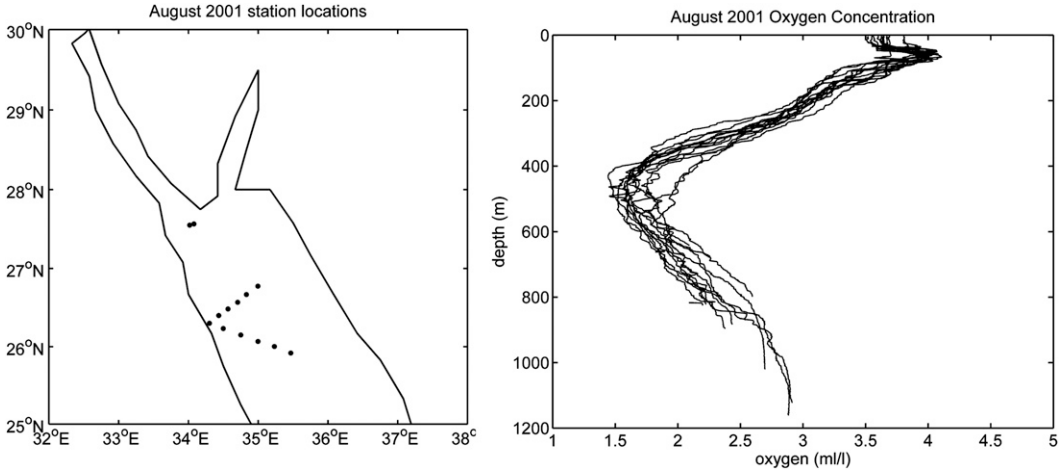

FIG. 13. (left) CTD stations over the northern Red Sea carried out in August 2001 and (right) the corresponding dissolved oxygen profiles.

maxima, are too small (one or two events for each case). More specifically, 50 out of the total 80 examined months have only events for one case (minima or maxima). For the other 30, in 20 cases minima and maxima have only one or two observed extremes with a time interval between them of more than 15 days. This is more evident when the 5th percentile criterion is employed for the extremes as Fig. 12 (bottom) shows. This suggests a ''persistence'' (blocking) of the atmospheric circulation pattern over long periods when minima or maxima of turbulent flux occur. The trends of the event number related to the 5th percentile are similar to those related to the deciles, though not significant at 95% confidence level.

It is well known that a consistent indicator of deep-water renewal over the global ocean is the concentration of dissolved oxygen. More specifically, a typical characteristic of recent deep-water formation is the finding of higher concentrations of dissolved oxygen values within the near-bottom water in comparison to the overlying layer. Although hydrographic observations in the Red Sea are limited, profiles of dissolved oxygen in the northern Red Sea typically show elevated concentrations in the near-bottom layer of the water column (see, e.g., Wyrtki 1974; Woelk and Quadfasel 1996; Sofianos and Johns 2007). Several profiles conducted in the Red Sea north of 25°N during the summer of 2001 from Sofianos and Johns (2007) are shown in Fig. 13. The vertical structure of the oxygen profiles indicates that the deep waters (deeper than 1000 m) should have recently been renewed by sinking of oxygen-enhanced surface waters, which became denser by strong surface cooling. This deep-water renewal is in accordance with the time plots of extremes and likely took place during the winter 2000/01, when several extreme events have been registered (Fig. 12, middle and bottom).

7. Concluding remarks

This study explored the large-scale atmospheric influence on the air–sea heat fluxes over the northern Red Sea during winter. We focus on the winter months (DJF) only, since during winter the important process of intermediate or deep convection potentially takes place over the northern part of the basin. The water convection ventilates the deeper layers and is a vital process for the entire basin ecosystem. Analysis carried out on the turbulent and radiative terms of the surface heat exchange showed that most of the winter flux variability is attributed to the turbulent flux's behavior. To examine the atmospheric forcing of this behavior, we have separated out the lowest and highest 5th percentiles of the daily turbulent values and created composite SLP maps corresponding to the minima and maxima of the turbulent fluxes. The resulting composites show distinct large-scale SLP patterns that affect the wind regime over the studied area. For the flux minima (extreme heat loss), the SLP field favors the transfer of dry and cold air masses from higher latitudes and creates a rather steep SLP gradient that generates strong winds. This SLP regime is associated with positive SLPA over the eastern Mediterranean, Turkey, northeastern Africa, and Middle East. In this way, the strong winds enhance the evaporation rate and lead to extreme heat loss from the sea surface. Conversely, the turbulent flux maxima (i.e., weak heat loss) are connected with a smooth SLP field over the northern Red Sea that leads to weak winds and positive heat flux anomalies. The large-scale SLPAs

present an almost zonal wavelike structure with successive opposite phases that alternate their sign between minima and maxima of the turbulent flux values. It has to be noted that this wavelike SLPA pattern is not directly related with one of the leading modes of SLP variability. Higher spatial correlations between the SLPA and three out of six EOFs indicates that a combination of these modes may explain the SLPA patterns associated with flux minima and maxima, although further research is required on this topic.

The temporal variability of the turbulent flux values shows a negative trend (i.e., enhanced heat loss), which is consistent with a positive SST trend over the entire basin (identified by Raitsos et al. 2011) if SST plays a primary role in the changing heat flux. A possible explanation of this finding is that sea surface warming takes place mostly over the southern part of the Red Sea Basin and travels to the north through the surface circulation. Subsequently, cold air outbreaks over the northern basin cause higher heat loss from the warmer water; further investigation is required to verify this suggestion. The temporal distribution of extreme events is in accordance with the negative turbulent fluxes trend as the number of weak heat loss episodes decreases with time and the number of strong heat loss episodes increases. Oxygen profiles from a cruise conducted during summer 2001 show recent deep-water renewal that is likely associated with strong cooling events that occurred in the previous winter.

The large-scale atmospheric circulation patterns that affect the heat flux minima and maxima display no obvious similarities with the primary modes of SLP variability. However, we have found a strong connection with the eastern Mediterranean lower-atmospheric circulation, which in turn is probably affected by well-known climatic indices, including the North Atlantic Oscillation, the east Atlantic pattern, and the east Atlantic–west Russia pattern. Given the geographic position of the Red Sea, it is possible that more climatic indices beyond the Eurasian region, in particular the El Niño–Southern Oscillation and the Indian monsoon index, may have a significant influence on the surface heat exchange of the basin. The study of how these climatic indices can affect the Red Sea heat budget is a topic of high importance and a challenge for a near-future investigation.

Acknowledgments. The authors acknowledge the Red Sea Research Center (RSRC) at King Abdullah University for Science and Technology (KAUST) for kindly sponsoring this study. Amy Bower was supported by Awards USA 00002, KSA 00011, and KSA 00011/02 made by KAUST to the Woods Hole Oceanographic Institution. We thank Dr. Sarantis Sofianos for generously sharing the hydrographic data reported in Sofianos and Johns (2007). Ping Zhai is also acknowledged for kindly producing the oxygen profiles figure. Three anonymous reviewers are acknowledged for their fruitful suggestions.

REFERENCES

Aiki, H., K. Takahashi, and T. Yamagata, 2006: The Red Sea outflow regulated by the Indian monsoon. *Cont. Shelf Res.,* **26,** 1448–1468.

Alexander, M. A., and J. D. Scott, 1997: Surface flux variability over the North Pacific and North Atlantic Oceans. *J. Climate,* **10,** 2963–2978.

Beal, L. M., A. Ffield, and A. L. Gordon, 2000: Spreading of Red Sea overflow waters in the Indian Ocean. *J. Geophys. Res.,* **105,** 8549–8564.

Biton, E., and H. Gildor, 2011: The coupling between exchange flux through a strait and dynamics in a small convectively driven marginal sea: The Gulf of Aqaba (Gulf of Eilat). *J. Geophys. Res.,* **116,** C06017, doi:10.1029/2011JC006944.

Bjornsson, H., and S. A. Venegas, 1997: A manual for EOF and SVD analyses of climate data. McGill University CCGCR Rep. 97-1, 54 pp.

Bond, N. A., and M. F. Cronin, 2008: Regional weather patterns during anomalous air–sea fluxes at the Kuroshio Extension Observatory (KEO). *J. Climate,* **21,** 1680–1697.

Bower, A. S., H. D. Hunt, and J. F. Price, 2000: Character and dynamics of the Red Sea and Persian Gulf outflows. *J. Geophys. Res.,* **105,** 6387–6414.

——, W. E. Johns, D. M. Fratantoni, and H. Petrs, 2005: Equilibration and circulation of Red Sea Outflow Water in the western Gulf of Aden. *J. Phys. Oceanogr.,* **35,** 1963–1985.

Cantin, N. E., A. L. Cohen, K. B. Karnauskas, A. M. Tarrant, and D. C. McCorkle, 2010: Ocean warming slows coral growth in the central Red Sea. *Science,* **329,** doi:10.1126/science.1190182.

Cayan, D. R., 1992: Latent and sensible heat flux anomalies over the northern oceans: The connection to monthly atmospheric circulation. *J. Climate,* **5,** 354–369.

Cember, R. P., 1988: On the sources, formation, and circulation of the Red Sea deep water. *J. Geophys. Res.,* **93,** 8175–8191.

Clifford, M., C. Horton, J. Schmitz, and L. H. Kantha, 1997: An oceanographic nowcast/forecast system for the Red Sea. *J. Geophys. Res.,* **102,** 25 101–25 122.

Dee, D. P., and Coauthors, 2011: The ERA-Interim reanalysis: Configuration and performance of the data assimilation system. *Quart. J. Roy. Meteor. Soc.,* **137,** 553–597.

Eshel, G., and N. Naik, 1997: Climatological coastal jet collision, intermediate water formation, and the general circulation of the Red Sea. *J. Phys. Oceanogr.,* **27,** 1233–1257.

——, M. A. Cane, and M. B. Blumenthal, 1994: Modes of subsurface, intermediate and deep water renewal in the Red Sea. *J. Geophys. Res.,* **99,** 15 941–15 952.

Fairall, C. W., E. F. Bradley, J. E. Hare, A. A. Grachev, and J. B. Edson, 2003: Bulk parameterization of air–sea fluxes: Updates and verification for the COARE algorithm. *J. Climate,* **16,** 571–591.

Fine, R., M. Warner, and R. Weiss, 1988: Water mass modification at the Agulhas retroflection: Chlorofluoromethane studies. *Deep-Sea Res. I,* **35,** 311–332.

Jiang, H., J. T. Farrar, R. C. Beardsley, R. Chen, and C. Chen, 2009: Zonal surface wind jets across the Red Sea due to mountain gap forcing along both sides of the Red Sea. *Geophys. Res. Lett.,* **36,** L19605, doi:10.1029/2009GL040008.

Josey, S. A., S. Somot, and M. Tsimplis, 2011: Impacts of atmospheric modes of variability on Mediterranean Sea surface heat exchange. *J. Geophys. Res.,* **116,** C02032, doi:10.1029/2010JC006685.

Kalnay, E., and Coauthors, 1996: The NCEP/NCAR 40-Year Reanalysis Project. *Bull. Amer. Meteor. Soc.,* **77,** 437–471.

Kendall, M. G., 1975: *Rank Correlation Methods.* Griffin, 196 pp.

Kleypas, J. A., G. Danabasoglu, and J. M. Lough, 2008: Potential role of the ocean thermostat in determining regional differences in coral reef bleaching events. *Geophys. Res. Lett.,* **35,** L03613, doi:10.1029/2007GL032257.

Leaman, K. D., and F. A. Schott, 1991: Hydrographic structure of the convection regime in the Gulf of Lions: Winter 1987. *J. Phys. Oceanogr.,* **21,** 575–598.

Mann, H. B., 1945: Nonparametric tests against trend. *Econometrica,* **13,** 245–259.

Morcos, S. A., 1970: Physical and chemical oceanography of the Red Sea. *Oceanogr. Mar. Biol. Annu. Rev.,* **8,** 73–202.

Murray, S. P., and W. Johns, 1997: Direct observations of seasonal exchange through the Bab el Mandeb Strait. *Geophys. Res. Lett.,* **24,** 2557–2560.

Papadopoulos, V. P., T. G. Chronis, S. Ruiz, E. Tragou, S. Josey, and G. Ferentinos, 2010: Air-sea heat fluxes estimation in the Aegean Sea (eastern Mediterranean). *Rapp. Comm. Int. Mer Mediterr.,* **39,** 156.

——, A. Bartzokas, T. Chronis, D. Georgopoulos, and G. Ferentinos, 2012a: Factors regulating the air–sea heat fluxes in the Aegean Sea. *J. Climate,* **25,** 491–508.

——, S. A. Josey, A. Bartzokas, S. Somot, S. Ruiz, and P. Drakopoulou, 2012b: Large-scale atmospheric circulation favoring deep- and intermediate-water formation in the Mediterranean Sea. *J. Climate,* **25,** 6079–6091.

——, H. Kontoyiannis, S. Ruiz, and N. Zarokanellos, 2012c: Influence of atmospheric circulation on turbulent air-sea heat fluxes over the Mediterranean Sea during winter. *J. Geophys. Res.,* **117,** C03044, doi:10.1029/2011JC007455.

Patzert, W. C., 1974: Wind-induced reversal in Red Sea circulation. *Deep-Sea Res.,* **21,** 109–121.

Plähn, O., B. Baschek, T. H. Badewien, M. Walter, and M. Rhein, 2002: Importance of the Gulf of Aqaba for the formation of bottom water in the Red Sea. *J. Geophys. Res.,* **107,** 3108, doi:10.1029/2000JC000342.

Raitsos, D. E., I. Hoteit, P. K. Prihartato, T. Chronis, G. Triantafyllou, and Y. Abualnaja, 2011: Abrupt warming of the Red Sea. *Geophys. Res. Lett.,* **38,** L14601, doi:10.1029/2011GL047984.

Shaman, J., R. M. Samelson, and E. Skyllingstad, 2010: Air–sea fluxes over the Gulf Stream region: Atmospheric controls and trends. *J. Climate,* **23,** 2651–2670.

Sofianos, S. S., and W. E. Johns, 2002: An oceanic general circulation model (OGCM) investigation of the Red Sea circulation, 1. Exchange between the Red Sea and the Indian Ocean. *J. Geophys. Res.,* **107,** 3196, doi:10.1029/2001JC001184.

——, and ——, 2003: An oceanic general circulation model (OGCM) investigation of the Red Sea circulation: 2. Three-dimensional circulation in the Red Sea. *J. Geophys. Res.,* **108,** 3066, doi:10.1029/2001JC001185.

——, and ——, 2007: Observations of the summer Red Sea circulation. *J. Geophys. Res.,* **112,** C06025, doi:10.1029/2006JC003886.

——, ——, and S. P. Murray, 2002: Heat and freshwater budgets in the Red Sea from direct observations at Bab el Mandeb. *Deep-Sea Res. II,* **49,** 1323–1340.

Tragou, E., C. Garrett, R. Outerbridge, and G. Gilman, 1999: The heat and freshwater budgets of the Red Sea. *J. Phys. Oceanogr.,* **29,** 2504–2522.

Woelk, S., and D. Quadfasel, 1996: Renewal of deep water in the Red Sea during 1982–1987. *J. Geophys. Res.,* **101,** 18 155–18 165.

Wyrtki, K., 1974: On the deep circulation of the Red Sea. *Processus de Formation des Eaux Oceaniques Profondes,* Colloques Internationaux 215, C.N.R.S., 91–106.

Yu, L., X. Jin, and R. A. Weller, 2007: Annual, seasonal, and interannual variability of air–sea heat fluxes in the Indian Ocean. *J. Climate,* **20,** 3190–3208.

——, ——, and ——, 2008: Multidecade global flux datasets from the objectively analyzed air-sea fluxes (OAFlux) project: Latent and sensible heat fluxes, ocean evaporation, and related surface meteorological variables. Woods Hole Oceanographic Institution OAFlux Project Tech. Rep. OA-2008-01, 64 pp.

Zhang, Y., W. B. Rossow, A. A. Lacis, V. Oinas, and M. I. Mishchenko, 2004: Calculation of radiative fluxes from the surface to top of atmosphere based on ISCCP and other global data sets: Refinements of the radiative transfer model and the input data. *J. Geophys. Res.,* **109,** D19105, doi:10.1029/2003JD004457.